

# Polarization of dust emission in clumpy molecular clouds and cores

T.J. Bethell, A. Chepurnov, A. Lazarian & J. Kim

## ABSTRACT

Grain alignment theory has reached the stage where quantitative predictions of the degree of alignment and its variations with optical depth are possible. With the goal of studying the effect of clumpiness on the sub-millimeter and far infrared polarization we computed the polarization due to alignment via radiative torques within clumpy models of cores and molecular clouds. Our models were based upon a highly inhomogeneous simulation of compressible magnetohydrodynamic turbulence. A Reverse Monte-Carlo radiative transfer method was used to calculate the the intensity and anisotropy of the internal radiation field, and the subsequent grain alignment was computed for a power-law distribution sizes using the DDSCAT package for radiative torques. The intensity and anisotropy of the intracloud radiation field show large variations throughout the models, but are generally sufficient to drive widespread grain alignment. The  $P - I$  relations for our models reproduce those seen in observations. We show that the degree of polarization observed is extremely sensitive to the upper grain size cut-off, and is less sensitive to changes in the radiative anisotropy. Furthermore, despite a variety of dust temperatures along a single line of sight through our core and amongst dust grains of different sizes, the assumption of isothermality amongst the aligned grains does not introduce a significant error. Our calculations indicate that sub-mm polarization vectors can be reasonably good tracers for the underlying magnetic field structure, even for relatively dense clouds ( $A_V \sim 10$  to the cloud center).

The current predictive power of the grain alignment theory should motivate future polarization observations using the next generation of multi-wavelength sub-mm polarimeters such as those proposed for SOFIA.

*Subject headings:* polarization, radiation mechanisms: general, ISM: magnetic fields, ISM: structure, infrared:ISM, submillimeter

## 1. INTRODUCTION

The role of magnetic fields in star formation has been the subject of heated debate (see McKee & Tan 2002, Ballesteros-Peredes et al. 2006). Polarization arising from aligned grains provides the most convenient way to study magnetic field topology within the clouds and cores and therefore helps to answer the questions facing the theorists.

Observations of polarized sub-mm emission from molecular clouds (Hildebrand et al. 2000 and references therein) are widely interpreted as emission from dust grains aligned with the local magnetic field. Advances in sub-mm technology have ensured that measurable degrees of polarization are seen in many interstellar clouds and cores (detections at the 0.5 – 8% level are typical, Dotson et al. 2006), as well as in a wide variety of other objects, such as circumstellar disks and the envelopes of young stellar objects. However, sub-mm polarimetry can only diagnose the magnetic field projected in the plane of the sky, and must be combined with other techniques to extract the full 3D magnetic field structure (see Yan & Lazarian 2006). Nevertheless, the ubiquity of both interstellar dust and magnetic fields ensures that the burgeoning field of sub-mm polarimetry is a profitable venture.

Substantial advancements in the grain alignment theory (see Lazarian 2003, for a review) have made it possible to predict the degrees of polarization and therefore compare theoretical and numerical models with observations. While simple models like those in Cho & Lazarian (2005, hereafter CL05) show a good correspondence between observations and theory, it is time to perform more sophisticated modeling to develop a more complete understanding of both dust grains and interstellar magnetic fields. This motivates our work below.

The challenge of understanding the theory behind polarization from aligned grains has been a significant one and much theoretical work has been done over the decades since the discovery of polarized starlight (Hall 1949, Hiltner 1949). Great minds like Edward Purcell and Lyman Spitzer worked productively in the field. Eventually, the original paradigm based on the paramagnetic alignment of grains (Davis & Greenstein 1967, Jones & Spitzer 1967, Purcell 1979, Spitzer & McGlynn 1979) was changed to one in which radiative torques played a major role. The picture that emerged seemed natural and self-consistent.

The alignment by radiative torques was first discussed in the 1970s. Dolginov & Mytrophanov (1976) proposed radiative torques as a mechanism that should naturally arise from the differential extinction of starlight (see also an earlier work by Dolginov 1972). However, it took 20 years for the mechanism to get its due recognition. This finally happened after Bruce Draine modified his open source DDSCAT code (Draine & Flatau 1994) to include the effect of radiative torques. In Draine & Weingartner (1996, 1997) the efficiency of radiative torques was proven for grains of rather arbitrary irregular shapes. However, alignment by

the paramagnetic mechanism was shown to be frustrated by the tendency of grains to flip (Lazarian & Draine 1999a,b).

Not only is the radiative torque mechanism attractive on theoretical grounds but it is also motivated by observations. For example, at the interface between diffuse and dense material ( $0 < A_V < 3$ ) in the Taurus Dark Clouds, Whittet et al. (2001) found that despite a uniform grain population, the peak near-infrared polarization wavelength correlated well with extinction. Lazarian (2003) explained this in terms of the natural extinction dependence of the radiative torque mechanism, preferentially aligning larger grains (which contribute to polarization at longer wavelengths) with increasing  $A_V$ .

In this paper we deal with the grain alignment in starless cores and in molecular clouds without bright OB stars. This is the case that challenges the theory to the utmost degree (see discussion in Lazarian, Goodman & Myers 1997). The original theoretical predictions for the radiative torques restricted the domain of radiative torques to  $A_V < 3$ , which made the observations of sub-mm polarization from cores with  $A_V > 10$  (Ward-Thompson et al. 2000, 2002) very surprising. However, CL05 showed that the efficiency of radiative torques *increases rapidly with grain size such that even a diluted and reddened intercloud radiation field can lead to grain alignment*. As it is well known that grains get bigger in molecular clouds, CL05 managed to address the aforementioned observational challenge.

In fact, CL05 performed the first detailed grain alignment calculation for a starless core model that included an accurate treatment of grain alignment via radiative torques. In lieu of a detailed grain alignment model, previous investigations have generally made *ad hoc* assumptions about the alignment of grains. For example, it has been assumed that all grains are aligned (Heitsch 2001), or in the case of Padoan et al. (2001) that there exists a critical extinction  $A_V \sim 3$  beyond which grain alignment is simply turned off. Without imposing these assumptions CL05 found that, provided there are large grains present, a significant degree of polarization may be detected from dark cores with extinctions as large as  $A_V = 10$ . Prior to modelling the polarization from particular objects CL05 determined the criterion for alignment, namely that the regular rotation rate arising from a balance between gaseous collisions and radiative torques must exceed the thermal tumbling rate of the grain. The ratio of these rates depends very sensitively upon grain size: in general there is a minimum grain radius for alignment,  $a_{alg}$ . For grains to be aligned they must be larger than  $a_{alg}$ . This requirement becomes increasingly difficult to meet when the radiation field is significantly extincted, since this reduces the radiative torques and implies a larger  $a_{alg}$ . With extinction comes reddening, which further diminishes the radiative torques acting on small grains, since grains couple with the radiation field most effectively when  $2\pi a \sim \lambda$ , where  $\lambda$  is the wavelength. Reddening increases the wavelengths at which most of the radiation is present

and thus increases  $a_{alg}$ . Also, increasing the density leads to an increase of the collision rate between grains and gas, which further increases  $a_{alg}$  since larger grains are less susceptible to these collisional events. CL05 gave an empirical formula which relates the minimum aligned grain size  $a_{alg}$  to the density  $n_H$  and extinction  $A_V$ ,

$$a_{alg} = (\log n_H)^3 (A_V + 5) / 2800, \quad (1)$$

where  $a_{alg}$  is in microns. Strictly speaking, this formula is only valid for the smooth, spherical clouds they considered, however it highlights the fact that increasing both the density and extinction inhibits grain alignment by increasing  $a_{alg}$ .

Despite the successes of their approach, CL05 lacked a detailed treatment of the radiative transfer, which (1) drives grain alignment, and (2) heats the dust grains, which subsequently reradiate the energy in the sub-mm. CL05 assumed a smooth 1D radially stratified core, adopting the radiation field of Mathis, Mezger & Panagia (1983) and a constant degree of anisotropy. They were able to show that the large grains hypothesized to exist in dense clouds are sufficiently sensitive to highly reddened, extinguished starlight to align with the magnetic field throughout their core. While the results are highly illustrative, one is left to wonder what role inhomogeneities play in *clumpy* prestellar cores. In what follows the term ‘clumpy’ shall be understood to mean structures with enhanced densities. These structures can loosely be categorized as sheets, filaments and cores, although we make no such distinction in this paper. As shown in Bethell et al. (2004) the radiation fields in a variety of clumpy clouds differ in a number of important respects from that in a uniform cloud. A few optically thin lines of sight allow considerable amounts of radiation to stream to great depths in clumpy objects with mean center-to-edge extinctions of  $A_V = 10$ . At these fiducial extinctions the radiation field is not only enhanced in intensity by orders of magnitude relative to the uniform case, but it is also considerably bluer. It is worth noting that introducing clumpiness leads to the possibility of self-shielding, sometimes rendering the *mass* less well illuminated than the *volume*, especially near the surface of the cloud. The principal purpose of this paper is therefore to extend the work of CL05 to the cases of clumpy clouds, treating the radiative transfer, dust heating and grain alignment in a detailed self-consistent manner using numerical methods.

This paper complements CL05 in the sense that combined they offer two extreme cases of cloud structure. We imagine that the results they yield should at least bracket those of real clouds. In order to understand what factors determine the observed polarization signal, we perform parameter studies. These involve varying the upper grain size limit  $a_{max}$ , the degree of anisotropy of the radiation field  $\gamma$ , and the grain temperatures  $T_g$ . It is often desirable

to estimate  $\gamma$  and  $T_g$  rather than calculate them in detail, and we explore what effects such simplifying assumptions have on the results. In general we find that the detailed properties of the radiation field inside our models are sufficient to produce widespread grain alignment. Despite the inhomogeneous conditions along any one line of sight through the core, we find that the observed polarization vectors are potentially useful tracers of the projected mass-averaged magnetic field over the range of column densities present in our clouds. Our polarization results should offer further encouragement to those exploring prestellar cores through polarized sub-mm emissions.

The structure of our paper is as follows. In §2 we describe our clumpy models, which are meant to represent a prestellar core and a larger molecular cloud. We also outline our choice of dust and interstellar radiation field. In §3 we give a brief description of the method we use to solve the radiative transfer equation in the turbulent core, and discuss the results relevant to grain heating and alignment via radiative torques. Section 4 deals with the alignment criterion for grains and their emission of polarized sub-mm radiation. Here we also discuss the basic polarization results for both our core and molecular cloud models in terms of polarization degree *versus* sub-mm intensity plots, the so-called ‘ $P-I$  relation’. We explore how our results are influenced by dust temperature, radiative anisotropies, and the limits imposed on the grain-size distribution. In §5 the polarization spectra for the models are shown, and we discuss how well polarization vectors align with the underlying projected magnetic field vectors. We discuss the implications of our results in §6.

## 2. THE CLUMPY MODELS

In this section we describe how we construct models of a prestellar core and a starless molecular cloud from a turbulent MHD simulation meant to represent a turbulently driven region of the ISM. While the limitations of the numerical simulations in terms of representing the actual interstellar turbulence, in particular, in terms of Reynolds and magnetic Reynolds numbers are well known (see Lazarian & Cho 2004), this does not compromise the goals of our study. Below we are not interested in the details of injection and dissipation of energy, but in finding to what extent the sub-mm polarimetry represents magnetic fields. For this purpose we concentrate on studying the effect of clumpiness on the observed polarization, which is the effect that is missing in the smooth CL05 model.

To simplify what follows, the density structures of both our clumpy core and molecular cloud models are based on a single three-dimensional simulation of turbulently driven MHD turbulence, described on a cubical grid with dimensions  $256 \times 256 \times 256$  cells. The simulation is described in detail in Vazquez-Semadeni et al. (2005). Here we briefly mention numerical

methods and parameters. We use a total variation diminishing scheme (Kim et al. 1999) for solving the isothermal MHD equations in a periodic computational box. The Poisson equation for the self-gravity of gas is solved by using the Fast Fourier Transform method. We drive a turbulent flow with the half scale of the size of one computational dimension, by adding velocity perturbations at an equal time interval. To achieve a high degree of clumpiness we adjust the velocity amplitude in such a way that the root-mean-square sonic Mach number is equal to around 10. The ratio of the initial magnetic pressure to gas pressure is 0.1. The strength of the magnetic field is in a magnetically supercritical range. The Jeans number, defined by the ratio of one dimensional size of the computational box to the Jean length, is 4.

We shall first discuss the construction of our core model. Although our turbulent simulation possesses the desired (large) degree of clumpiness, it is also statistically homogeneous and therefore not a good model for a prestellar core. As a rule, cores obtained with direct numerical simulations are small and rather smooth, and do not allow the studies that we have in mind. Therefore, instead of using a brute force approach, we create a model core combining numerical simulations and information obtained from observations.

Self-gravitating cores, although poorly resolved in observations, exhibit central density peaks and lower density envelopes. To improve our model we use the statistically homogeneous yet clumpy density structure and follow CL05 by imposing both a spherical outer boundary and a radial envelope profile. The underlying turbulent density continuum is multiplied by the radial envelope function to endow the cloud with a *mean* radial profile<sup>1</sup> consistent with observations (Tafalla et al. 2004). The envelope function is defined as;

$$\rho(r) \propto \begin{cases} \text{const} & \text{if } r < r_0/4.7, \\ r^{-1} & \text{otherwise.} \end{cases}$$

where the radius  $R$  of the cloud is  $R = 24r_0 = 0.02\text{pc}$ , and  $r$  is measured from the center of the core. The spherical, radially stratified, turbulent density continuum is then normalised such that the mean visible band *center-to-edge* extinction is  $A_V = 10$ , corresponding to a column density of  $N_H \sim 1.7 \times 10^{22}\text{cm}^{-2}$  and mean volume density  $\langle n_H \rangle \sim 1.3 \times 10^5\text{cm}^{-3}$ . Both the physical size and mean column density are consistent with the cores L183, L1544 and L43 observed in Crutcher et al. (2004). The column density map of the core and its projected magnetic field are shown in Figure 1. The projected mass-weighted magnetic field structure has been smoothed by a beamwidth equivalent to 1/32 of the map width. From the column density map it is clear that the large density fluctuations in this particular MHD

---

<sup>1</sup>The mean radial profile is the average density in thin shells of radii  $r$  centered on the core center.

simulation overwhelm the imposed radial density gradient. While low mass prestellar cores of this sort do not exhibit the large supersonic linewidths present in the underlying MHD simulation, there is evidence that they are clumpy nevertheless. The turbulent structure in this case can be considered a proxy for clumpiness arising from the evolution of localised gravitational collapse<sup>2</sup>.

When the opacity simply scales with density, as it does in our case, the radiative transfer equation becomes a function of column density only. Provided we preserve the column density structure, the internal radiation field and any related quantities which do not depend explicitly on density can then be used for a large family of objects; from small dense cores to larger, more diffuse molecular clouds. Exploiting this fact we rescale our model core to larger physical dimensions and reciprocally decrease its density, such that the column density is held constant,  $N_H = \langle n_H \rangle R = \text{constant}$ . Thus, from our model core we create a complementary molecular cloud model with mean density  $\langle n_H \rangle = 10^3 \text{cm}^{-3}$  and physical size  $R = 2.6 \text{pc}$ . The column density map and magnetic field structure of the molecular cloud model are identical to that shown for the core in Figure 1. Not only will the internal mean intensity and its anisotropy be the same for both models, but the resulting temperatures of comparable dust grains (if present) will also be the same. In order to exploit this invariance between core and molecular cloud we have implicitly assumed that the extinction curves underlying the radiative transfer through the two models are identical. This is unlikely to be exactly true since dust evolves according to its environment (Mathis 1990), the primary effect of which is observed as a change in the ratio of total to selective extinction,  $R_V \equiv A_V/E(B - V)$ . In dense objects the small grains tend to grow through coagulation, resulting in a flatter extinction curve and a larger  $R_V$ . This inconsistency may not prove to be problematic since the radiation field in clumpy objects is determined by radiation streaming through optically thin windows. This radiation typically carries a relatively weak imprint of the extinction curve; it is the geometry rather than extinction curve which dominates the transfer of radiation. For comparably clumpy clouds, Bethell et al. (2006) have shown that varying  $R_V$  from 3.1 to 5.5 changes the intracloud V-band radiation field by less than a factor of 2. This is in stark contrast to the case of uniform clouds, where the internal radiation field is highly sensitive to the adopted value of  $R_V$  (Cecchi-Pestellini et al 1995).

---

<sup>2</sup>An alternative approach to defining a core would be to extract a core from a self-gravitating MHD simulation. The MHD simulation used in this paper is not sufficiently evolved to produce a large number of such cores, and the cores that are produced are not well resolved numerically. For the purposes of calculating the internal radiation field it is important to resolve all structures down to scales corresponding to an optical depth of order unity. For this reason we use the entire MHD simulation to construct our core.

## 2.1. Dust properties

To calculate as self-consistently as possible the attenuation of the interstellar radiation field by dust, the subsequent equilibrium dust temperatures, and the sub-mm emission, we use a detailed dust grain ensemble composed of two materials; pure ‘astronomical’ silicate and pure graphite (Draine & Lee 1984)<sup>3</sup>. In order to form a grain population it is necessary to apply a size distribution to the individual grains; we select the simple power-law grain size distribution of Mathis, Rumpl & Nordsieck (1977, hereafter MRN),

$$n(a) = A_{g,s} a^{-3.5} \quad (2)$$

where  $a$  is the grain radius, and  $n(a)da$  the number density of grains with radii in the interval  $[a, a+da]$ . The  $A_{g,s}$  are the MRN abundance factors for silicates ( $s$ ) and graphite ( $g$ ). Our adopted default lower and upper grain size cutoffs (for both graphite and silicate) are  $a_{min} = 0.01\mu\text{m}$  and  $a_{max} = 2\mu\text{m}$  respectively for the model core, and  $a_{min} = 0.005\mu\text{m}$  and  $a_{max} = 0.5\mu\text{m}$  for the molecular cloud model. In order to adjust the limits of the grain size distribution one must simultaneously ensure that the total dust mass is conserved, which one can do by simply rescaling  $A_{g,s}$ . In the MRN distribution the total number of dust grains is determined by  $a_{min}$ , while the total mass in dust  $M_{dust}$  is determined largely by  $a_{max}$ , provided  $a_{max} \gg a_{min}$ ;

$$M_{dust} \propto \int_{a_{min}}^{a_{max}} A n(a) a^3 da \propto A a_{max}^{0.5}. \quad (3)$$

In order to avoid violating the total metal abundance we conserve  $M_{dust}$  by requiring that  $A \propto a_{max}^{-0.5}$ . This point is largely irrelevant to this paper, since we concern ourselves primarily with *relative* abundances of small and large grains, rather than their total abundances.

The resulting grain populations produce extinction curves with total-to-selective extinction ratios of  $R_V \sim 4$  and  $5.5$  for the model molecular cloud and core respectively. The upper grain size limit  $a_{max}$  is rather larger than that presented in the original MRN. In the dense ISM, dust grains are expected to increase their size through coagulation (Clayton & Mathis 1988, Vrba et al. 1993) and mantle growth (e.g. Barlow 1978). By considering only large grains we restrict ourselves to the sub-mm realm of dust emission. Shortward of  $\lambda \sim 100\mu\text{m}$  dust emission is dominated by very small grains heated stochastically to high temperatures

---

<sup>3</sup>Tabulated optical properties may be found at the website [www.astro.princeton.edu/~draine](http://www.astro.princeton.edu/~draine).

by single ultraviolet (UV) photons (e.g. Draine & Li 2001). The emission in the spectral regime dominated by stochastic grain-heating is not well modelled by grains in thermal equilibrium, the approximation we use in this paper, and which is only valid for the regime in which large grains dominate the sub-mm emission ( $\lambda > 100\mu\text{m}$ ). However, such heating is essentially irrelevant for our models if we assume a sufficient depletion of very small grains.

Once the dust ensemble is fully prescribed and the ambient radiation field known, it is then possible to calculate the equilibrium grain temperature and spectral emissivity of each grain type and grain size at each location in the core. At sub-mm wavelengths the core is optically thin and the effects of absorption and scattering on the emergent sub-mm flux can be ignored.

## 2.2. The interstellar radiation field

Since our models are starless, the only permeating radiation field is that of the highly diluted starlight which pervades the Galaxy. The interstellar radiation field impinging upon our core is that of Mathis, Mezger & Panagia (1983) and consists of a superposition of three diluted blackbody spectra and a small ultraviolet feature. The blackbody temperatures are  $T = 3000, 4000$  and  $7500\text{K}$ , and their respective dilution factors  $W = 4 \times 10^{-13}, 1 \times 10^{-13}$  and  $1 \times 10^{-14}$ . These values are approximately valid for the ISRF located at a Galactic radius  $r_G = 5\text{kpc}$ . Additionally, we adopt the simplifying assumption that the field is homogeneous and isotropic in the vicinity of our core. In reality a small degree of intrinsic anisotropy ( $\sim 10\%$ ) and inhomogeneity is expected in the ISRF, resulting from the complex transfer of starlight through the Galaxy as a whole. To simplify the radiative transfer through our core we ignore this small intrinsic anisotropy, considering it to be of secondary importance to the effects of clumpiness.

## 3. RADIATIVE TRANSFER

It is here that our method differs most significantly from those in CL05. In CL05 both the impinging and internal radiation fields were simply taken from Mathis, Mezger & Panagia (1983), which was possible because in one dimensional models the radiation field is a function of  $A_V$  only (defined inwards from the cloud surface). In order to calculate the penetration of our clouds by the ISRF we use the three dimensional reverse Monte Carlo numerical method described in Bethell et al. (2004). The *reverse* Monte Carlo scheme is based upon the reciprocity principle (Case 1957) and differs from the more conventional

*forwards* scheme (e.g. Witt 1977) in that it grows probabilistic photon trajectories in a backward fashion. We start a reverse trajectory at what is its final physical destination  $\mathbf{x}$  and direction  $\mathbf{k}$ , evolving it probabilistically until it reaches the external source of photons (the ISRF). It is therefore well suited to describing not only the mean intensity but also the angular distribution of the intensity  $I(\mathbf{k}, \mathbf{x})$  at any chosen point. The moments of the radiation field, and in particular the degree of anisotropy (described later), are obtained straightforwardly from  $I(\mathbf{k}, \mathbf{x})$ . Trajectories are generated until  $I(\mathbf{k}, \mathbf{x})$  meets a prescribed signal-to-noise criterion (in this paper the Monte Carlo noise levels are uniformly kept below 1%). Algorithmic control of the signal-to-noise ratio is of particular importance for dense, self-shielding clumps where most of the mass resides, because these may be relatively poorly explored in simple forwards Monte Carlo schemes.

The individual trajectories are constructed from contiguous line segments, the length of each is a probabilistic sampling of the optical depths due to pure scattering, while the angles between segments are drawn probabilistically from the scattering redistribution function. The redistribution function is taken to be the popular Henyey-Greenstein function (Henyey & Greenstein 1941). While not the most sophisticated phase function (Witt 1977, Draine 2003) it encapsulates the essential features of scattering, and takes a conveniently compact mathematical form. It is described by one parameter, the scattering anisotropy  $g = \langle \cos \theta \rangle$ , which lies in the interval  $[-1, 1]$  where  $g = -1$  represents backwards scattering,  $g = 0$  isotropic scattering, and  $g = 1$  forwards scattering. While observations of reflection nebulae and diffuse Galactic emission (Gordon 2004 and references therein) place constraints on the dust albedo  $\omega$  and anisotropy parameter  $g$ , the important role of inhomogeneities tends to increase the uncertainties in the values derived from radiative transfer modelling (Mathis, Whitney & Wood 2002). For the dust ensemble described in 2.1 the values of  $g$  are typically forward throwing, ranging from 0.5 in the visual to 0.75 in the UV.

The quantity most relevant to grain heating is the specific mean intensity, defined as;

$$J_\lambda(\mathbf{x}) = \frac{1}{4\pi} \int I_\lambda(\mathbf{k}, \mathbf{x}) \, d\Omega, \quad (4)$$

where  $\Omega$  is the solid angle in steradians. The radiative equilibrium temperature  $T_g$  of an individual dust grain is determined by balancing the absorbed radiation (UV-visible) with that emitted in the sub-mm (see equation 6.2 in Draine & Lee 1984). By integrating the spectral emissivity  $j_\lambda(a, T_g, \mathbf{x})$  over the dust size distribution we obtain the total spectral emissivity  $j_\lambda(\mathbf{x})$  in  $\text{ergs cm}^{-3} \text{sterad}^{-1} \text{cm}^{-1}$ .

In order to compute the radiative torque acting on a dust grain we first calculate the spectral degree of anisotropy of the radiation field  $\gamma_\lambda(\mathbf{x})$ , given by;

$$\gamma_\lambda(\mathbf{x}) = \frac{1}{4\pi J_\lambda(\mathbf{x})} \left| \int I_\lambda(\mathbf{k}, \mathbf{x}) \mathbf{k} d\Omega \right|. \quad (5)$$

The spectral degree of anisotropy  $\gamma_\lambda(\mathbf{x})$  lies in the range  $[0, 1]$ , where 0 corresponds to an isotropic field and 1 to a unidirectional field; in essence it measures the directionality of the radiation field. We further simplify  $\gamma_\lambda(\mathbf{x})$  by defining the wavelength independent bolometric anisotropy;

$$\gamma(\mathbf{x}) = \frac{\int \gamma_\lambda(\mathbf{x}) J_\lambda(\mathbf{x}) d\lambda}{\int J_\lambda(\mathbf{x}) d\lambda}, \quad (6)$$

which also lies in the range  $[0, 1]$ , and is the quantity used in the radiative torque calculations in Section 4. The UV-visible anisotropy in a clumpy medium depends largely on the clumpy geometry, rather than the wavelength dependent properties of dust scattering. In this case the anisotropy is approximately wavelength independent and  $\gamma_\lambda(\mathbf{x}) \sim \gamma(\mathbf{x})$  for most wavelengths.

### 3.1. Results

Before proceeding with calculations of grain alignment and polarized dust emission it is worth considering some of the underlying radiative transfer results. In Figure 2 we show comparative slices of the density continuum  $n_H(\mathbf{x})$ , the internal mean intensity  $J_\lambda(\mathbf{x})$ , and the anisotropy  $\gamma_\lambda(\mathbf{x})$ , evaluated at  $\lambda = 0.54\mu\text{m}$ . The morphology of the radiation field is of interest, as it indicates which environments possess favorable conditions for grain alignment. In a uniform cloud  $J_\lambda(\mathbf{x})$  decreases in a quasi-exponential manner with increasing depth from the cloud surface (Flannery et al. 1980). In the clumpy cloud we generally see a much weaker variation with radial position, and a more appreciable anticorrelation with density. The radiation field floods the available volume, illuminating the surfaces of clumps deep inside the cloud. Much of the attenuation of the radiation field occurs in the envelopes of our self-shielding clumps, where  $J_\lambda(\mathbf{x})$  may drop precipitously by several orders of magnitude. The heirarchical structure of our clumpy cloud ensures that the densest points are the most shielded, and extremely large extinctions can occur over small distances in the vicinity of clumpy structures. The model mass and volume fractions as functions of  $J_V$  are shown in the top panel of Figure 3. In the lower panel we show the mean overdensity of material associated with a value of  $J_V$ , which illustrates clearly the effect of self-shielding. The very darkest locations are on average about ten times denser than the global mean density. Referring back to Figure 2 we see that the degree of anisotropy shows morphologically very

little correlation with density, and tends to be largest on the *surfaces* of sheets, filaments and clumps, where gradients in  $n_H$  and  $J_\lambda(\mathbf{x})$  are usually large. It is worth noting that the anisotropies found in clumpy clouds are not necessarily larger than those found in uniform clouds. In a uniform spherical cloud there is always a single well-defined ‘brightest direction’ (except at the cloud center): the anisotropy  $\gamma \sim 0.5$  at the cloud surface, initially increasing slightly with depth, only to decrease towards  $\gamma = 0$  at the cloud center. In contrast, the anisotropy in the clumpy cloud shows little radial dependence. Instead, the anisotropy at a point is dominated by a few beams of starlight distributed quasi-randomly in the sky. These fluxes tend to average out somewhat, resulting in rather small mass-averaged anisotropies of  $\gamma \sim 0.34$ . To illustrate this point, we plot the mass and volume fractions as a function of  $\gamma$  in Figure 4. Both curves are peaked at  $\gamma \sim 0.3$ , although the mass fraction curve is slightly broader. The similarity between the mass and volume-weighted curves indicates that there is little overall correlation between density and anisotropy. Furthermore, the anisotropy varies by less than an order of magnitude, generally falling within the range  $\gamma = 0.1 - 0.6$ . These values are somewhat lower than the constant value  $\gamma = 0.7$  adopted by CL05 and Draine & Weingartner (1996) for their dense clouds. In a later section we shall explore how assuming a spatially uniform value for  $\gamma$  affects the polarized emission.

The temperature distributions of graphite grains with radii  $a = 0.01, 0.1$  and  $1.0\mu\text{m}$  are shown in Figure 5. The inefficiency with which small grains emit sub-mm radiation accounts for the systematic increase of grain temperature with decreasing grain radius. Furthermore, small grains preferentially absorb the bluer part of the ISRF, which, due to the steep increase of extinction with decreasing wavelength, is subject to the largest spatial variations inside the core. The relatively wide temperature distribution of these small grains reflects this sensitivity. The assumption of isothermal dust temperatures is therefore best applied when the emission is dominated by the large grains (i.e. at  $\lambda > 300\mu\text{m}$ ). At shorter wavelengths the emission is dominated by the warm, small grains, and the extraction of useful physical properties of a cloud is complicated by the need to know the temperature distribution of the grains (Hildebrand 1983, Chen 1990, Li et al. 1999, Schnee et al. 2006). In later sections we shall explore the effect an isothermal dust temperature assumption has on the polarization degree.

#### 4. GRAIN ALIGNMENT AND POLARIZED SUB-MM EMISSION

We are now in a position to begin calculating grain alignment and the polarized emission from these grains. For the relatively large grains we consider in this work, the damping of a constant radiative torque leads to a grain spinning with a steady angular frequency  $\Omega_{rad}$ .

However, in the absence of a strong radiative torque one would expect collisions with gaseous atoms to cause the grain to rotate irregularly with an angular velocity  $\Omega_{th}$ , corresponding to a kinetic energy  $\sim kT/2$ . Only when the grain is rotating suprathermally, i.e.  $\Omega_{rad} > \Omega_{th}$ , will the damping from gaseous collisions be insufficient to prevent the grain from aligning with the magnetic field. Following CL05 we consider a grain to be aligned with the magnetic field if its angular frequency of rotation is greater than the thermal value by a factor of three, i.e.  $\Omega_{rad}/\Omega_{th} > 3$ . The ratio  $\Omega_{rad}/\Omega_{th}$  is given by;

$$(\Omega_{rad}/\Omega_{th})^2 = \frac{5\alpha_1}{192\delta_2} \left(\frac{1}{n_H kT}\right)^2 \frac{\rho a_{eff}}{m_h} \left[ \int d\lambda Q_\Gamma \lambda (4\pi\gamma J_\lambda/c)^2 \right] \left( \frac{1}{1 + \tau_{d,gas}/\tau_{d,em}} \right)^2 \quad (7)$$

where  $a_{eff}$  is the effective grain cross-section, and  $\tau_{d,gas}/\tau_{d,em}$  is the ratio of gas drag to thermal emission drag times. The quantities  $c$  and  $k$  are the speed of light and Boltzmann's constant respectively. The radiative torque efficiency,  $Q_\Gamma$ , is calculated using the discrete dipole code DDSCAT (Draine & Flatau 2004). The anisotropy and mean intensity appear in the integral as the product  $\gamma J_\lambda$ , and this along with  $Q_\Gamma$  determines the strength of the radiative torque. The smallest grain size for which the above criterion is met is denoted by  $a_{alg}$ . Typically, grains of radii larger than  $a_{alg}$  will be aligned with the magnetic field, while smaller grains will not. When a grain is considered aligned we assume its alignment with the magnetic field is perfect.

Having defined the condition for grain alignment, we proceed to calculate the polarization signal arising from the thermal emission of the spinning grains. At sub-mm wavelengths the core is optically thin to the emitted radiation from dust, and to a good approximation the emergent sub-mm intensity is simply the integral of the dust emissivity along a line of sight through the cloud. Following Fiege & Pudritz (2000), we write out the Stokes parameters of the emitted radiation as functions of plane-of-sky coordinates  $(\psi, \phi)$ :

$$Q = \int n_H G_{pol} \cos 2\psi \cos^2 \phi dz, \quad (8)$$

$$U = \int n_H G_{pol} \sin 2\psi \cos^2 \phi dz, \quad (9)$$

and

$$I = \int n_H G_{ran} dz - \int n_H G_{pol} \left( \frac{1}{2} \cos^2 \phi - \frac{1}{3} \right) dz. \quad (10)$$

The density  $n_H$  is the appropriate weighting for the dust emission along the line of sight, since the dust-to-gas ratio is assumed to be constant. The quantity  $\psi$  is the angle between the plane-of-sky projection of the magnetic field and north, and  $\phi$  is the angle between the magnetic field and the picture plane. The polarized and unpolarized components of the emissivity are respectively

$$G_{pol} = \sum_i \sigma_{pol,i} \int_{a_{align,i}}^{\infty} a^3 B_{\lambda}(T_g) n_i(a) da \quad (11)$$

and

$$G_{ran} = \sum_i \sigma_{ran,i} \int_0^{\infty} a^3 B_{\lambda}(T_g) n_i(a) da, \quad (12)$$

where  $B_{\lambda}(\lambda)$  is the blackbody function. As described in Section 2.1  $n_i(a)$  is the grain number density. The following approximation is used in eqns 11 and 12 to simplify the sub-mm emission efficiencies of the grains;

$$C_{X,i} = \sigma_{X,i} \lambda^{-2} a^3, \quad a \ll \lambda \quad (13)$$

where  $X$  denotes either the polarized (*pol*) or random (*ran*) components, and the index  $i$  denotes silicate (*s*) or graphite (*g*). For this calculation the relative abundances of the polarizing and non-polarizing cross-sections (Lee & Draine 1984) are related via  $\sigma_{pol,s}/\sigma_{ran,s} = 0.67$ ,  $\sigma_{ran,g}/\sigma_{ran,s} = 1.60$ , and  $\sigma_{pol,g} = 0$ . Here we have assumed that the graphite grains do not align with the magnetic field. The degree of polarization  $P$  follows from the Stokes vector,

$$P = \frac{\sqrt{Q^2 + U^2}}{I}. \quad (14)$$

Wherever alignment prevails we assume it is perfect, and the angle  $\theta$  between the grain angular momentum vector and the magnetic field is zero. The Rayleigh reduction factor,  $R = 1.5(< \cos^2 \theta > -1/3)$ , which measures the effective degree of alignment between the population of grains and magnetic field, is simply reinterpreted as the fraction of the total emissive dust cross-section associated with aligned grains;

$$R = \frac{\int_{a_{alg}}^{a_{max}} C_{ran} n(a) da}{\int_{a_{min}}^{a_{max}} C_{ran} n(a) da}. \quad (15)$$

By increasing  $a_{max}$  we increase this fraction. The Rayleigh reduction factor is now a function of position on our core;  $a_{alg}$  is the smallest grain which satisfies the alignment criterion  $\Omega_{rad}/\Omega_{th} > 3$ , and so depends on the local radiation field and density.

#### 4.1. Results for the model core

Our default core model has the density structure described in Section 2, and an MRN grain size distribution with  $a_{max} = 2\mu\text{m}$ . The anisotropy and mean intensity of the internal radiation field (see Section 3) is used to determine the alignment and polarized emission from grains throughout the model. Unless otherwise stated the results are made at an observational wavelength of  $850\mu\text{m}$ . The emission map of our default core model, including polarization vectors, is shown in Figure 6. The polarization vectors have been smoothed in a similar manner to the projected magnetic field, i.e. by a beamwidth equal to  $1/32$  of the map width. The differences between the  $850\mu\text{m}$  map and those computed at other wavelengths of interest, such as  $350$  and  $450\mu\text{m}$ , are visually very minor. In what follows we consider  $850\mu\text{m}$  our default wavelength. Comparing the  $850\mu\text{m}$  map with the column density  $N_H$  and projected magnetic field (see Figure 1) we see that the sub-mm emission map correlates well with the column density. This can be explained by noting that  $850\mu\text{m}$  is in the Rayleigh-Jeans spectral regime, combined with the fact that the large grains responsible for the sub-mm emission possess a narrow distribution in temperature (see Figure 5). Under these circumstances the volumetric emissivity (in units of  $\text{ergs s}^{-1} \text{ cm}^{-3} \mu\text{m}^{-1}$ ) is almost directly proportional to the density,  $n_H$ .

Sub-mm observations often reveal various “depolarization” effects, especially towards the centers of strong sub-mm emission (Gonçalves, Galli & Walmsley 2005). This appears as an empirical anticorrelation between the polarization degree  $P$  and the sub-mm intensity  $I$ , and which is usually fitted with a power-law  $P \propto I^{-\alpha}$  (Henning et al. 2001, Lai et al. 2003, Crutcher et al. 2005). The index  $\alpha$  is seen to vary considerably between cores, typically taking values in the range 0.6-1.2 (Matthews & Wilson 2000, 2002, Henning et al. 2001, Lai et al. 2003, Crutcher et al. 2004). In the case of  $\alpha > 1$  the polarized intensity  $I_p = PI$  *decreases* towards bright sub-mm regions. The  $P - I$  scatter for our core is shown in the lefthand panel of Figure 7. Qualitatively it exhibits the observed  $P - I$  anticorrelation, although there is also a large scatter about this trend. Similar plots were produced in CL05 showing a tighter correlation, primarily due to the smoothness of their cores. On the other hand the periphery of our core exhibits so-called “polarization limb brightening”, in which the conditions for alignment are favorable (i.e. a strong radiation field and appreciable

anisotropy) and the line of sight passes through only a short section of material. These points represent the upper limit in the  $P - I$  relation at small  $I/I_{max}$ .

CL05 showed that the power-law index  $\alpha$  is strongly dependent on the upper cutoff in the grain size distribution  $a_{max}$ . Considering that the largest grains are typically the first to be aligned, increasing  $a_{max}$  above the threshold for alignment  $a_{alg}$  increases the fraction of the grain population for which the alignment criterion (equation 7) is met. In the dense, dark clumps into which longer wavelength radiation penetrates, only the very largest grains are expected to be aligned via radiative torques. Under these circumstances increasing  $a_{max}$  produces preferentially more polarization in regions of strong sub-mm emission. This is observed as a flatter  $P - I$  relation, characterized by smaller values of  $\alpha$ . It is important to clarify exactly how much of this relation is due to the efficiency of grain alignment via radiative torques, as opposed to effects attributable to changes in the magnetic field orientation along lines of sight. In other words, what is the maximum observable polarization that can be obtained from this core? To address this question we recalculate the polarization map at  $850\mu\text{m}$  *with all silicate grains aligned*, the result of which is shown in the right panel in Figure 7. In this case the scatter and  $P - I$  relation is due to geometrical depolarization effects along each line of sight, and represents the maximum possible observational polarization we can obtain from the model. In particular one should note that at large  $I/I_{max}$  some of the reduction in polarization must be caused by the magnetic field morphology changing along the lines of sight.

#### 4.1.1. Effect of changing $a_{max}$ , $\gamma$ and $T_g$

Central to this paper is the detailed calculation of the anisotropy  $\gamma(\mathbf{x})$  and dust grain temperatures  $T_g(\mathbf{x})$ . Before we explore the sensitivity of our results to these quantities, we first consider the effects of changing the upper grain-size limit  $a_{max}$ . The existence of sufficiently large grains is essential if the radiative torque mechanism is to produce detectable degrees of polarization ( $P > 1\%$ ). The extinction properties of dust in the very dense ISM suggest that the grain size distribution extends to larger  $a_{max}$ , which is believed to be due to the process of grain coagulation. The original MRN distribution which reproduces the average Galactic extinction curve has a sharp cutoff at  $a_{max} = 0.25\mu\text{m}$ , although more recent distributions include an exponential tail of large grains extending up to  $a > 1\mu\text{m}$  (Weingartner & Draine 2001). Provided the grain size distribution extends beyond the minimum aligned grain size  $a_{alg}$ , i.e.  $a_{max} > a_{alg}$ , a fraction of the grains will be aligned and we can expect a non-zero degree of polarization.

The  $P - I$  relations obtained using different values of  $a_{max}$  are shown in Figure 8. It

is clear from this figure that increasing  $a_{max}$  increases the polarization degree. Regions of high column density (i.e. the bright sub-mm regions) benefit most from the increase in  $a_{max}$  since these regions are expected to be the least well illuminated by an anisotropic radiation field, and an increase in  $a_{max}$  under these conditions can make the difference between having some grains aligned ( $a_{max} > a_{alg}$ ) and having no grains aligned ( $a_{max} < a_{alg}$ ).

We can explore the effects of changing  $\gamma(\mathbf{x})$  by recalculating the polarization with constant values for the anisotropy,  $\gamma = 0.1, 0.3$  and  $1.0$ , covering the range of real values (the real mass averaged anisotropy is  $\gamma_m \sim 0.34$ , see Figure 4). The resulting  $P - I$  relations are shown in the bottom panel of Figure 8. Although changing  $\gamma$  in this way does little to the scatter in the  $P - I$  relation it is clear that it affects the overall scaling. For  $\gamma = 0.1$  (consistent with the intrinsic anisotropy of the Galactic ISRF) the radiative torques are suppressed to such an extent that few of the grains responsible for the  $850\mu\text{m}$  emission are aligned and  $P < 1\%$ . With  $\gamma = 0.3$  the results are quite similar to those obtained with the real  $\gamma(\mathbf{x})$  values, and a significant fraction of the cloud has a degree of polarization above  $1\%$ . With the maximal anisotropy,  $\gamma = 1.0$ , we see a further increase in  $P$ , the upper envelope of which is now above  $1\%$  over the entire range of observed  $I/I_{max}$ .

The narrow temperature distribution of large grains (see Figure 5) suggests that temperature variations amongst the grains emitting most of the  $850\mu\text{m}$  emission are small and relatively unimportant. Indeed, if we recompute the polarization degree using  $T = 10\text{K}$  for all grains regardless of size or location, we obtain a result almost indistinguishable from that using the physically derived grain temperatures  $T_g(a, \mathbf{x})$ . This discrepancy is shown in histogram form in Figure 9. The ‘isothermal’ approximation leads to small errors (generally no larger than  $0.2\text{dex}$ ) in the  $850\mu\text{m}$  polarization signal.

## 4.2. Results for the molecular cloud model

The main differences between the molecular cloud and core models are the densities involved and the range of  $a_{max}$  considered. Our molecular cloud model has  $a_{max} = 0.5\mu\text{m}$  and a mean density of  $n_H = 10^3\text{cm}^{-3}$ , and exploits the same radiation field and dust temperatures used in our core model. The  $P - I$  relation for our molecular cloud model is shown in the top panel of Figure 10. In the lower panel we show the maximal polarization arising when all silicate grains are aligned with the magnetic field. It is informative to compare these results with those for the default core model in Figure 7. The two  $P - I$  relations are qualitatively similar, although it seems that a slightly larger degree of polarization is obtained at large  $I/I_{max}$  from our default molecular cloud model. As described in Section 4, a reduction in  $n_H$  reduces the disalignment arising from collisions between grains and gas-phase particles.

This favors grain alignment by lowering  $a_{alg}$  (see equation 1). Although the model molecular cloud has fewer large grains ( $a_{max} = 0.5\mu\text{m}$ ) it seems that the concomitant reduction in  $a_{alg}$  is more than enough to compensate. Applying equation 1 we see that reducing the density by a factor of 130 (which is required in order to turn our core into the molecular cloud) leads to a factor of  $\sim 10$  decrease in  $a_{alg}$ . This is larger than the factor of 4 decrease in  $a_{max}$  (from  $2\mu\text{m}$  to  $0.5\mu\text{m}$ ). As a result a larger fraction of the grains in the molecular cloud are aligned. We now perform a brief parameter study to see how sensitive these results are to our default values.

#### 4.2.1. Effect of changing $a_{max}$ , $\gamma$ and $T_g$

The top panel of Figure 11 shows the effects of changing  $a_{max}$  over the range  $[0.25, 0.75]\mu\text{m}$ . Once again, a larger  $a_{max}$  leads to a larger polarization degree and flatter  $P - I$  relation in bright sub-mm regions. Even the modest change from  $a_{max} = 0.25\mu\text{m}$  to  $0.5\mu\text{m}$  leads to a several-fold increase in  $P$ . The bottom panel in Figure 11 shows the effects of imposing a uniform anisotropy,  $\gamma = 0.1, 0.3$  or  $1.0$ . As expected, the assumption of uniformity and the value adopted for  $\gamma$  has less of an effect than the choice of  $a_{max}$ . Once again, assuming that the grains responsible for the  $850\mu\text{m}$  polarized emission emit isothermally at 10K introduces only a small error, as seen in Figure 9.

## 5. SPECTRUM AND ALIGNMENT OF POLARIZATION

In this section we consider two different types of spectra formed from the polarized emission; first a spectrum of the polarized intensity, and second, a spectrum of the polarization degree. The latter is known as the ‘polarization spectrum’, the form of which is highly indicative of the source of the polarized emission. It helps discriminate between populations of warm and cold aligned grains, which may, for example, imply the presence of additional grain alignment via localised star formation.

The map-averaged spectrum of the polarized intensity is presented in Figure 12. The polarized intensity deviates very little from the spectrum obtained with a population of large grains emitting at  $T = 10\text{K}$ , which is approximately consistent with the mean temperature for the largest aligned grains (see Figures 5 and 9). In our models the grains exhibit a range of temperatures ( $\Delta T_g \sim 4\text{K}$ ) which explains why our curve is broader than the isothermal 10K curve. In our molecular cloud model, the aligned grains are smaller and therefore also warmer on average than those responsible for the polarized emission in the model core. As

a result the polarized intensity spectrum for the molecular cloud is shifted towards slightly shorter wavelengths, although the effect is rather subtle. As was shown in section 4.1.1 the small temperature fluctuations along a random line of sight have very little effect on the emergent polarization degree. Instead the temperature range merely acts to broaden the polarized intensity spectrum.

The map-averaged degree of polarization as a function of wavelength (the polarization spectrum) for both our models are shown in Figure 13. Superposed are the wavebands frequently observed from the ground (350, 450 and 850 $\mu\text{m}$ ), as well as the projected wavelength range for the Hale polarimeter (promising a wavelength coverage of 53 – 215 $\mu\text{m}$ , Hildebrand, private communication), one of the polarimeters proposed for SOFIA. For wavelengths longer than  $\sim 400\mu\text{m}$  the mean polarization degree is constant at  $\sim 2 - 2.5\%$ , dropping precipitously at wavelengths less than 350 $\mu\text{m}$  where the small, unaligned grains begin to dominate the sub-mm emission.

### 5.1. Alignment of polarization and magnetic field

The angle  $\theta$  between the polarization and projected magnetic field vectors is an indicator of the ability of polarization maps to reveal the projected structure of the underlying magnetic field. We obtain  $\cos^2 \theta$  from the dot product of the polarization and projected magnetic field vectors,

$$\cos^2 \theta = \left( \frac{\mathbf{P} \cdot \mathbf{B}_{\text{proj}}}{|\mathbf{P}| |\mathbf{B}_{\text{proj}}|} \right)^2, \quad (16)$$

where  $\mathbf{B}$  is the mass weighted projected magnetic field. An informative quantity is the degree of alignment as a function of column density. The most natural way to express the degree of alignment is through the mean  $\cos^2 \theta$ , since this appears in the conventional definition of the Rayleigh reduction factor (see Section 4). In Figure 14 the mean quantity  $\langle \cos^2 \theta \rangle$  is shown as a function of  $N_H$  for both our models. Although these results are calculated at the default wavelength (850 $\mu\text{m}$ ), the following results do not change significantly with wavelength. The alignment is approximately constant,  $\langle \cos^2 \theta \rangle \sim 0.75$ , throughout the range of column densities, although there is a large scatter about this average value. If  $\mathbf{P}$  and  $\mathbf{B}_{\text{proj}}$  were randomly oriented with respect to one another we would expect  $\langle \cos^2 \theta \rangle = 0.5$ . From these results it seems that the polarization vectors do on average trace the projected magnetic field vectors over the range of column densities. The map-averaged  $\cos^2 \theta$  is shown as a function of wavelength in Figure 15. There is no significant dependence on wavelength

from  $\lambda = 100 - 1000\mu\text{m}$ .

## 6. Discussion

By considering very clumpy models for prestellar cores and molecular clouds we found that:

1. Detectable levels of polarization ( $P > 1\%$ ) should be present from clumpy, optically thick ( $A_V \sim 10$ ) prestellar cores and turbulent molecular clouds. The alignment of large grains ( $a \sim 1\mu\text{m}$ ) via the mechanism of radiative torques is shown to be an effective process in our models, even though the only source of radiation is the mean interstellar radiation field. However, the presence of sufficiently large grains is essential for this mechanism to work efficiently.

2. The inclusion of clumpiness and a detailed solution of the radiative transfer equation does not significantly change the qualitative nature of the results described in CL05. In addition, we note that the distribution in temperatures of the large, aligned grains is very narrow and the assumption of isothermality amongst these grains introduces only a negligibly small error into the polarization calculation.

3. The emergent degree of polarization is only moderately sensitive to simplifying assumptions about the radiative anisotropy. However, it is extremely sensitive to the adopted upper cut-off of the power-law distribution of grain sizes.

4. Despite the highly complex magnetic field geometry in our clumpy models, the polarization vectors trace the mass-weighted projected magnetic field vectors reasonably well, even for lines of sight where  $A_V \sim 10$ .

5. The synthetic polarization spectra are flat longward of  $\lambda \sim 300\mu\text{m}$  but fall precipitously shortward of this wavelength. This is in part due to an absence of emission at these short wavelengths. Multi-frequency polarimetric studies as well as new models are necessary to further test the theory of grain alignment via radiative torques.

Many extensions to this work are also possible; for example, the eventual onset of star formation in our core will introduce local sources of highly anisotropic radiation. These stars will illuminate the dense clumps from within, where grain alignment from the ISRF alone might prove inadequate. The polarization due to embedded stars will typically produce a different polarization spectrum, introducing a warm component extending to smaller grain sizes. The detailed effects of embedded star-formation are to be considered in a future paper. Indeed, observed polarization spectra show an increase in polarization degree shortward of

$300\mu\text{m}$ , which can be most easily attributed to an additional population of warm, aligned grains. Since we only include the basal ISRF our calculations lack both sufficiently warm grains and the diversity of conditions that prevail in real objects such as M17 and OMC-1 (Vaillancourt 2002). For these reasons we do not expect our current models to exactly reproduce the observations shortward of  $300\mu\text{m}$ .

Given that appreciable polarization signals arise in even our conservative models, it seems reasonable to assume that a measurable polarization should be found throughout the lifetime of a core. The polarization degree arising from the radiative torque mechanism is determined by the largest grains, and is therefore sensitive to the upper grain-size limit  $a_{max}$ . If constraints can be placed on the ambient radiation field then the polarization degree could be an effective probe of the large grains in the interstellar dust population. Such favorable conditions should prevail in the vicinity of individual or compact clusters of stars where the radiative anisotropy is approximately unity.

Due to poor sub-mm wavelength coverage, it is currently difficult to draw strong conclusions about the physical conditions in a cloud from the observed polarization spectra (e.g. Hildebrand et al. 2000). However, a number of sub-mm telescopes and detectors are planned for the near future (e.g. Planck, Herschel, SOFIA), many of which will eventually have polarimetric capabilities. In particular, SOFIA (the Stratospheric Observatory for Infrared Astronomy), once equipped with a polarimeter such as Hale, will dramatically enhance our ability to map the magnetic field structure in prestellar cores, as well as a variety of other environments. Measurements shortward of  $300\mu\text{m}$  in a diverse sample of objects should prove particularly useful, since it is here that our models predict a rapid decline in the polarization degree. Explaining the discrepancy between our models and observations in this spectral regime will be a strong test of the radiative torque theory. Thus, the need for spectropolarimetry is clear: not only is a broad wavelength coverage required in order to describe the polarization spectrum, but spectral information is essential for disentangling the various physical environments that may exist along any given line of sight (Chen 1990, Xie et al. 1991, Hildebrand et al. 1999). Furthermore, our paper shows that a reliable statistic of the magnetic field topology can be obtained via sub-mm polarimetry. Comparing these predictions with observations will provide a valuable test for the grain alignment theory. As a consequence of such testing we will not only gain insight into the physics of star-formation but also gain confidence in future studies of magnetic fields in circumstellar environments, comet coma and tails, and other galaxies (see Lazarian 2003).

While in the above work we disregard both paramagnetic alignment pioneered by Davis-Greenstein (1951) and mechanical alignments pioneered by Gold (1952), we believe that our estimates above will not be substantially altered if we include these mechanisms. As

discussed in Lazarian et al. (1997) the conditions within the molecular clouds are close to equilibrium ones. Thus without radiative torques the grains rotate essentially thermally. As the gas and grain temperatures are not very different in molecular clouds, the paramagnetic alignment is marginal, even if grains have superparamagnetic properties (see Roberge & Lazarian 1999). The relative gas grain velocities that are necessary for the mechanical alignment are dominated by the gyroresonance acceleration (Yan & Lazarian 2003). For molecular clouds the resulting velocities are not high enough, however (see Yan, Lazarian & Draine 2004) to produce efficient mechanical alignment (see Roberge, Hanany & Messinger 1995, Lazarian 1997 and references therein).

After this paper was written we learned about the interesting and complementary work of Pelkonen et al. (2006), which also extends the CL05 model by applying it to numerical simulations. In contrast to our work, Pelkonen et al. study much smoother cores in the context of their parental cloud. We restrict ourselves to one isolated core model, but calculate its polarized sub-mm emission in great detail. Pelkonen et al. assume a constant degree of anisotropy of  $\gamma = 0.7$  (e.g. Draine & Weingartner 1996) which is a factor of two larger than our mass-averaged value. In the context of their smooth cores this approximation may prove to be adequate, although in our calculations the properties of the anisotropy are rather different. Despite our detailed calculations it is still not clear how to prescribe approximate values for  $\gamma$  on the basis of the density structure alone. Despite these uncertainties, Pelkonen et al. also show, as we have done in this paper, that the observed  $P - I$  relations can be reproduced within the radiative torque framework.

Interestingly, Pelkonen et al. directly employ the empirical formula for the radiative torque given by equation 1. This is possible if the intracore radiation field can be described by a single effective extinction  $A_V$ . Their approach is therefore a direct application of the CL05 method to 3D cloud structures. In our model, because of its extreme clumpiness, the radiation field cannot be described by a single parameter (like  $A_V$ ) and requires detailed calculation. Unfortunately it seems unlikely that a simple empirical formula for the radiative torque exists for highly clumpy objects such as ours. Despite their differences these two complementary approaches represent the first attempts at developing the radiative torque mechanism for inhomogeneous media, and there is still much interesting work to be done in this area.

TJB is happy to acknowledge support provided by the NASA ATP program and NSF grant (AST 0507367). AL acknowledges the support by the NSF grants AST 0098597, AST 0243156 and AST 0507164, as well as by the NSF Center for Magnetic Self-Organization in Laboratory and Astrophysical Plasmas, AC acknowledges the support by the NSF grant AST 0507164.

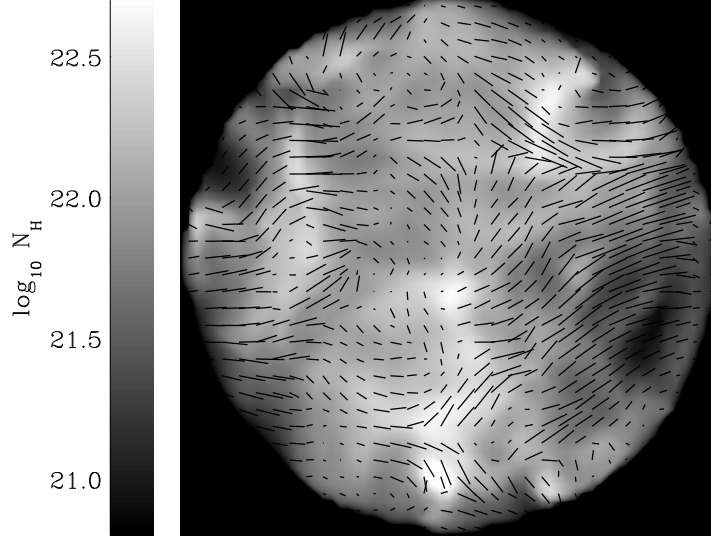


Fig. 1.— The column density  $N_H$  of the model core (and molecular cloud). The projected mass-weighted magnetic field vectors are shown superposed.

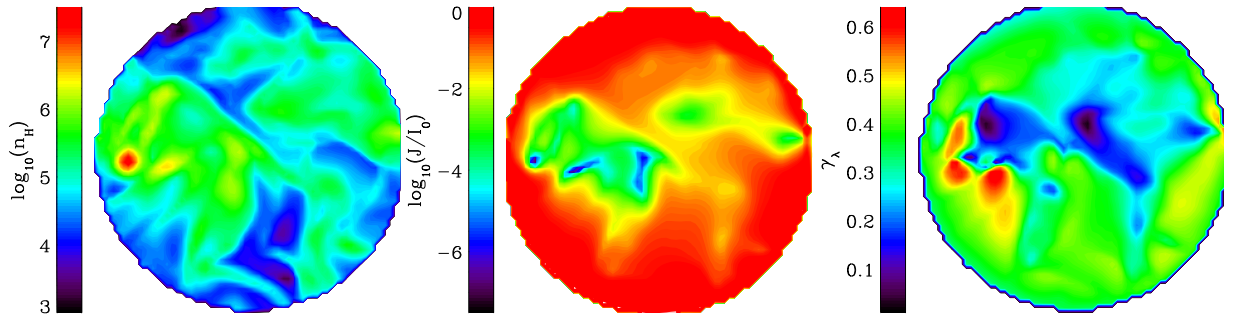


Fig. 2.— *Left*: a slice through the density continuum of our model core. The corresponding slice through the molecular cloud model is identical except that the densities are a factor of 130 smaller. *Center*: the same slice through the internal mean intensity  $J_\lambda$  at  $\lambda = 0.54\mu\text{m}$ , normalised to the value of the unattenuated ISRF,  $I_0$ . *Right*: the anisotropy of the radiation field,  $\gamma$ , at  $0.54\mu\text{m}$ .

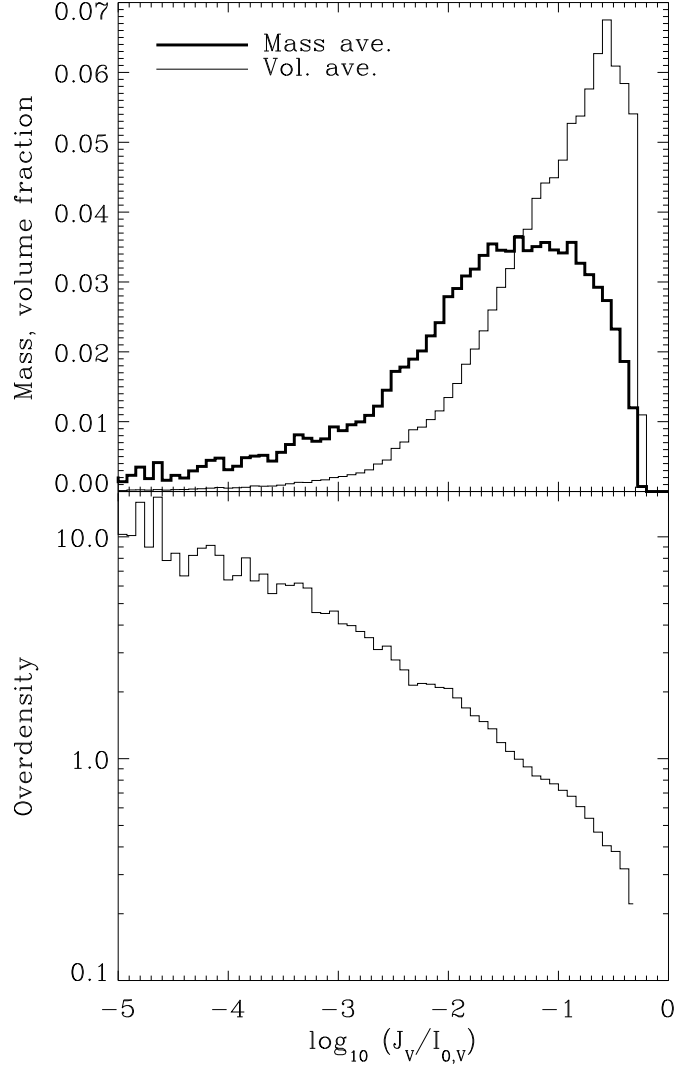


Fig. 3.— *Top panel:* The fractions of the mass (*thick line*) and volume (*thin line*) associated with an internal V-band relative mean intensity  $J_V/I_{0,V}$ . The quantity  $I_{0,V}$  is the unattenuated ISRF intensity. *Bottom panel:* The mean overdensity (i.e. the mass fraction divided by the volume fraction) as a function of the mean intensity. For example, the overdensity indicates that material bathed in radiation for which  $\log_{10}(J_V/I_{0,V}) = -4$  is, on average, seven times more dense than the global average density. Each bin is 0.08dex in width.

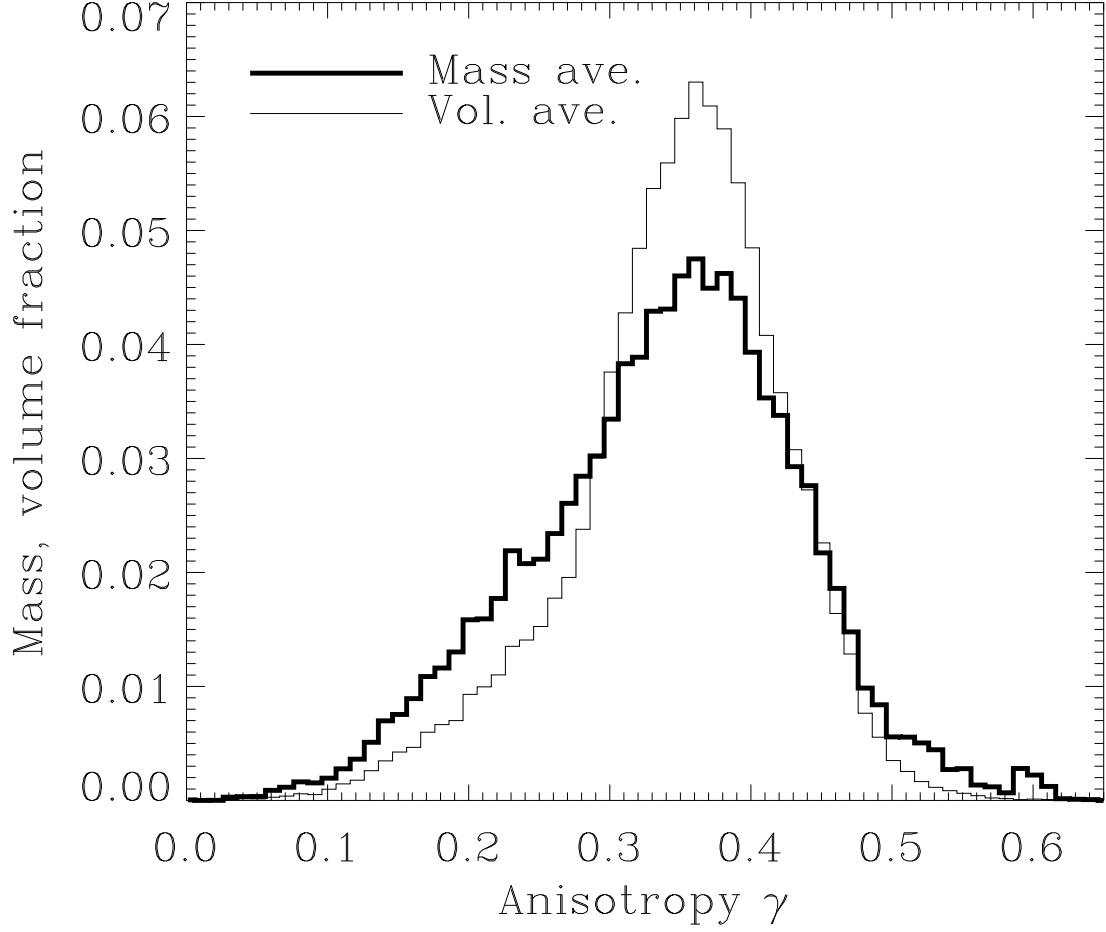


Fig. 4.— The mass (*thick line*) and volume (*thin line*) fractions associated with a radiative anisotropy  $\gamma$ . Both the mass and volume averaged anisotropies are approximately equal at  $\gamma_{m,v} \sim 0.34$ .

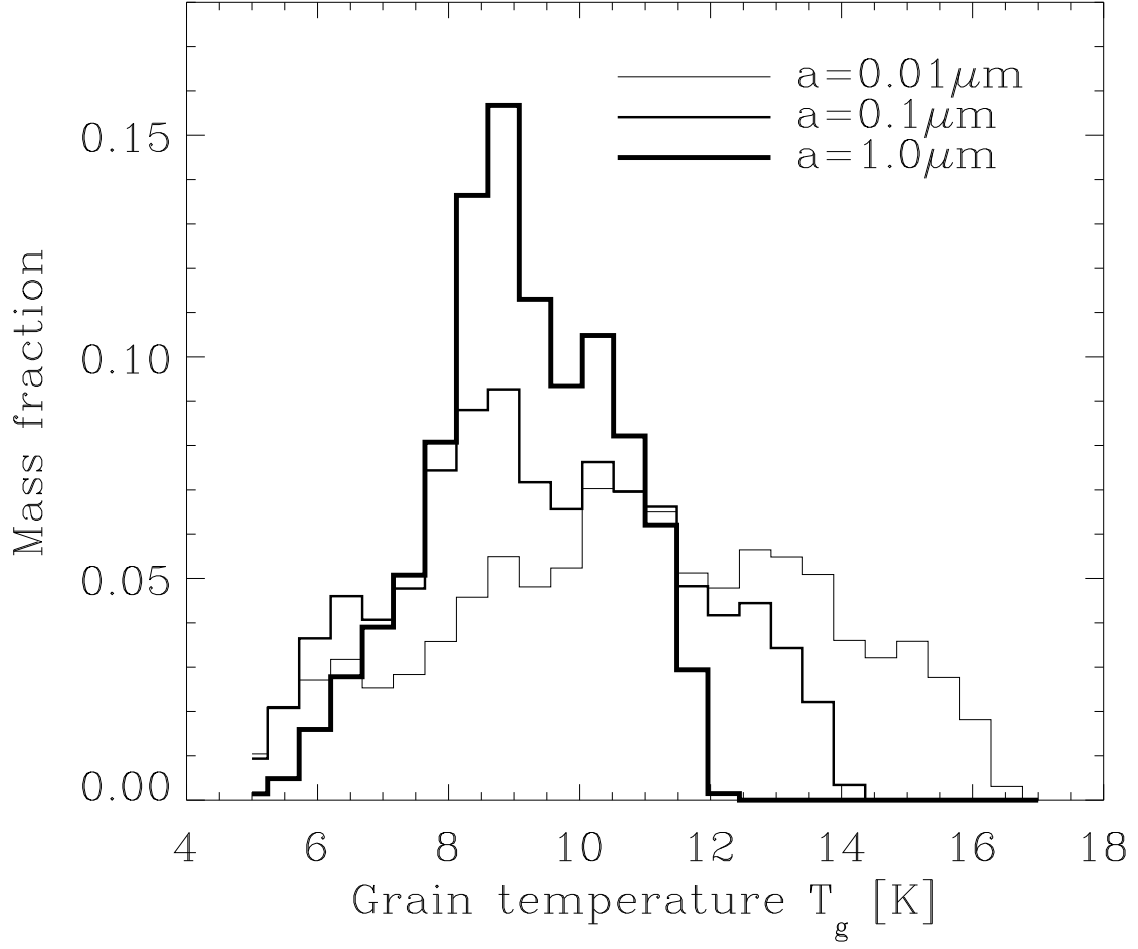


Fig. 5.— The distribution of mass with silicate grain temperature for grains of radii  $a = 0.01, 0.1$  and  $1.0 \mu\text{m}$ . The binsize is  $0.48\text{K}$ .

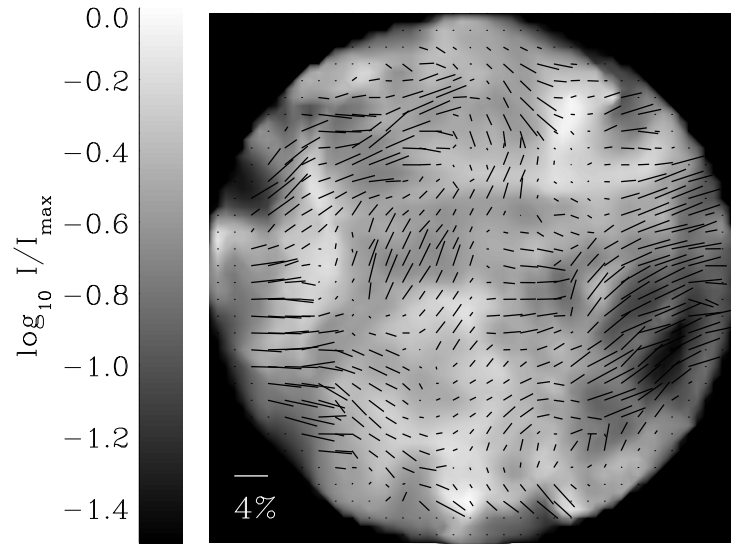


Fig. 6.— The  $850\mu\text{m}$  emission map of the model core. Superposed are the projected polarization degree vectors. A 4% polarization vector is shown for scale.

## REFERENCES

- Ballesteros-Paredes, J., Klessen, R.S., Mac Low M., Vazquez-Semadeni E. 2006, in Protostars and Planets V, astro-ph/0603357
- Barlow, M. J. 1978, MNRAS, 183, 417
- Bethell T.J. , Zwiebel E.G. ,Heitsch F. ,Mathis J. , 2004, ApJ, 610, 812
- Bethell T.J. , Zwiebel E.G. , Li, P.S. 2006, ApJin press
- Cardelli, J. A., Clayton, G. C., & Mathis, J. S. 1989, ApJ, 345, 245
- Case, K. M. 1957, Reviews of Modern Physics, 29, 651
- Cecchi-Pestellini, C., Aiello, S., & Barsella, B. 1995, MNRAS, 274, 134
- Chen, N.-X. 1990, Physical Review Letters, 64, 1193
- Cho J. , Lazarian A. , 2005, ApJ, 631, 361, CL05
- Clayton, G. C., & Mathis, J. S. 1988, ApJ, 327, 911
- Crutcher, R. M., Nutter, D. J., Ward-Thompson, D., & Kirk, J. M. 2004, ApJ, 600, 279
- Davis, L. & Greenstein, J.L. 1951, ApJ, 114, 206
- Dolginov A.Z. 1972, Ap&SS, 16, 337
- Dolginov, A. Z., & Mytrophanov, I. G. 1976, Ap&SS, 43, 291
- Draine B.T. , 2003, Annu. Rev. Astron. Astrophys., 41, 241
- Draine, B.T., and Flatau, P.J. 2004, "User Guide to the Discrete Dipole Approximation Code DDSCAT 6.1", <http://arxiv.org/abs/astro-ph/0409262>
- Draine, B. T., & Lee, H. M. 1984, ApJ, 285, 89
- Draine, B. T., & Li, A. 2001, ApJ, 551, 807
- Draine B.T. , Weingartner, J., 1996, ApJ, 470, 551
- Draine, B. T., & Weingartner, J. C. 1997, ApJ, 480, 633
- Fiege J.D. , Pudritz R.E. , 2000, ApJ, 544, 830

- Flannery, B. P., Roberge, W., & Rybicki, G. B. 1980, *ApJ*, 236, 598
- Gold, T. 1952, *Nature*, 169, 322
- Gonçalves, J., Galli, D., & Walmsley, M. 2005, *A&A*, 430, 979
- Gordon, K. D. 2004, *ASP Conf. Ser.* 309: *Astrophysics of Dust*, 309, 77
- Hall, J. S. 1949, *Science*, 109, 166
- Henning, T., Wolf, S., Launhardt, R., & Waters, R. 2001, *ApJ*, 561, 871
- Heitsch, F., Zweibel, E. G., Mac Low, M.-M., Li, P., & Norman, M. L. 2001, *ApJ*, 561, 800
- Heney, L. G., & Greenstein, J. L. 1941, *ApJ*, 93, 70
- Hildebrand, R. H. 1983, *QJRAS*, 24, 267
- Hildebrand, R. H., Dotson, J. L., Dowell, C. D., Schleuning, D. A., & Vaillancourt, J. E. 1999, *ApJ*, 516, 834
- Hildebrand, R. H., Davidson, J. A., Dotson, J. L., Dowell, C. D., Novak, G., & Vaillancourt, J. E. 2000, *PASP*, 112, 1215
- Hiltner, W. A. 1949, *Science*, 109, 165
- Jones, R.V. & Spitzer, L. 1967, *ApJ*, 147, 943
- Kim, J., Ryu, D., Jones, T. W., & Hong, S. S. 1999, *ApJ*, 514, 506
- Lai, S.-P., Girart, J. M., & Crutcher, R. M. 2003, *ApJ*, 598, 392
- Lazarian, A. 1994, *MNRAS*, 268, 713
- Lazarian, A. 1997, *ApJ*, 483, 296
- Lazarian, A. 2003, *Journal of Quantitative Spectroscopy and Radiative Transfer*, 79, 881
- Lazarian, A., Goodman, A.A., & Myers, P.C. 1997, *ApJ*, 490, 273
- Lazarian, A., & Cho, J. 2004, *Ap&SS*, 292, 29
- Lazarian, A., & Draine, B. T. 1999a, *ApJ*, 516, L37
- Lazarian, A. & Draine, B. 1999b, *ApJ*, 520, L67
- Lazarian, A., & Roberge, W. G. 1997, *ApJ*, 484, 230

- Lee, H. M., & Draine, B. T. 1985, *ApJ*, 290, 211
- Li, D., Goldsmith, P. F., & Xie, T. 1999, *ApJ*, 522, 897
- McKee, Christopher F.; Tan, Jonathan C. 2002, *Nature*, 416, 59
- Mathis, J., S., Mezger, P., G., & Panagia, N., 1983, *A&A*, 128, 212
- Mathis, J. S. 1990, *ARA&A*, 28, 37
- Mathis, J. S., Rumpl, W., & Nordsieck, K. H. 1977, *ApJ*, 217, 425
- Mathis, J. S., Whitney, B. A., & Wood, K. 2002, *ApJ*, 574, 812
- Matthews, B. C., & Wilson, C. D. 2000, *ApJ*, 531, 868
- Matthews, B. C., & Wilson, C. D. 2002, *ApJ*, 574, 822
- Padoan, P., Goodman, A., Draine, B. T., Juvela, M., Nordlund, Å., Rognvaldsson, Ö. E. 2001, *ApJ*, 559, 1005
- Purcell, E. 1979, *ApJ*, 231, 404
- Purcell, E. & Spitzer, L. 1971, *ApJ*, 167, 31
- Roberge, W., Hanany, S., & Messinger, D. 1995, 453, 238
- Roberge, W.G., & Lazarian, A. 1999, *MNRAS*, 305, 615
- Schnee, S., Bethell, T., & Goodman, A. 2006, *ApJ*, 640, L47
- Spitzer, L. & McGlynn, T. 1979, *ApJ*, 231, 417
- Tafalla, M., Myers, P. C., Caselli, P., & Walmsley, C. M. 2004, *A&A*, 416, 191
- Vaillancourt, J. E. 2002, *ApJS*, 142, 53
- Vázquez-Semadeni, E., Kim, J., Shadmehri, M., & Ballesteros-Paredes, J. 2005, *ApJ*, 618, 344
- Vrba, F. J., Coyne, G. V., & Tapia, S. 1993, *AJ*, 105, 1010
- Ward-Thompson, D., Kirk, J.M., Crutcher, R.M., Greaves, J.S., Holland, W.S., & Andre, P. 2000, *ApJ*, 537, L135
- Ward-Thompson, D., Andre, P., & Kirk, J. 2002, *MNRAS*, 329, 257

- Weingartner, J., C., & Draine, B., T., 2001, ApJ, 548,296
- Whittet, D. C. B., Gerakines, P. A., Hough, J. H., & Shenoy, S. S. 2001, ApJ, 547, 872
- Witt, A. N. 1977, ApJS, 35, 1
- Xie, T., Goldsmith, P. F., & Zhou, W. 1991, ApJ, 371, L81
- Yan, H. & Lazarian, A., 2006, ApJ, in press
- Yan, H. & Lazarian, A. 2003, ApJ, 592, 33
- Yan, H., Lazarian, A., & Draine, B. 2004, ApJ, 616, 895

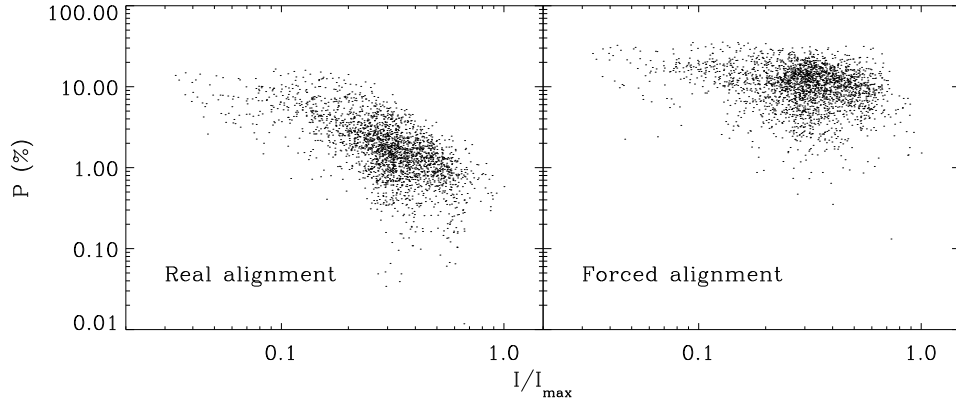


Fig. 7.— *Left*): The polarization degree,  $P$ , as a function of normalized intensity,  $I/I_0$ , for our core model. This calculation uses the full, detailed internal radiation field and dust temperatures. *Right*): The P-I relation obtained when all silicate grains are forced into alignment with the magnetic field. Each dot represents a line of sight through the cloud, or equivalently a pixel in Figure 6. These polarization degrees are evaluated at the default wavelength of  $850\ \mu\text{m}$ .

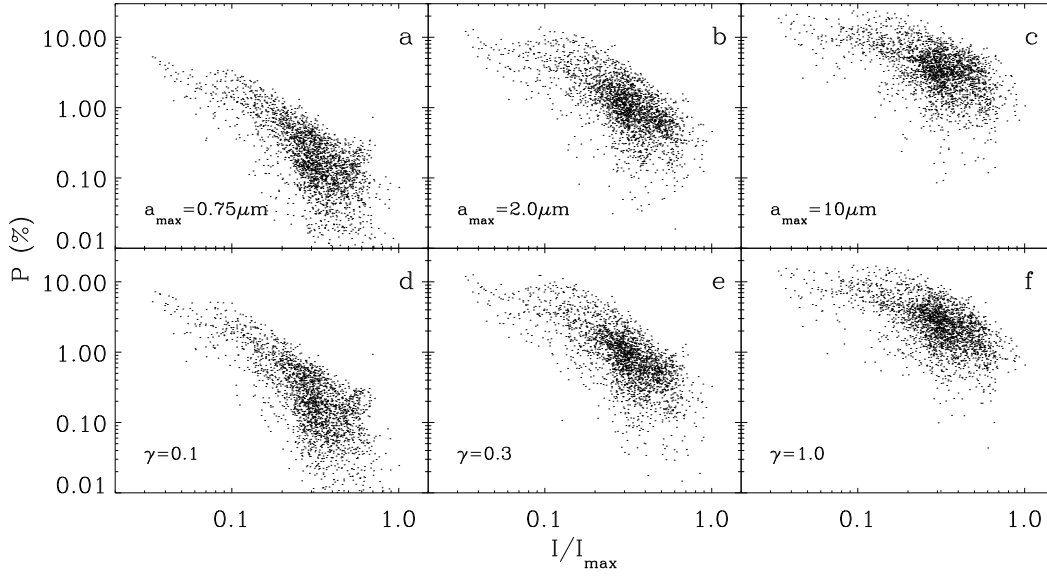


Fig. 8.— P-I plots for the model core obtained from the parameter study. The top row (a-c) shows how varying the upper grain-size cutoff,  $a_{\max}$ , changes the P-I relation. Plot *b* is in fact the result for our default core model. In the bottom row (d-f) we have replaced the real, spatially varying values for the radiative anisotropy,  $\gamma$ , with constant values  $\gamma = 0.1, 0.3$  and  $1.0$ . For comparison, the true mass averaged anisotropy is  $\gamma_m = 0.34$ . These plots are evaluated at  $850 \mu\text{m}$ .

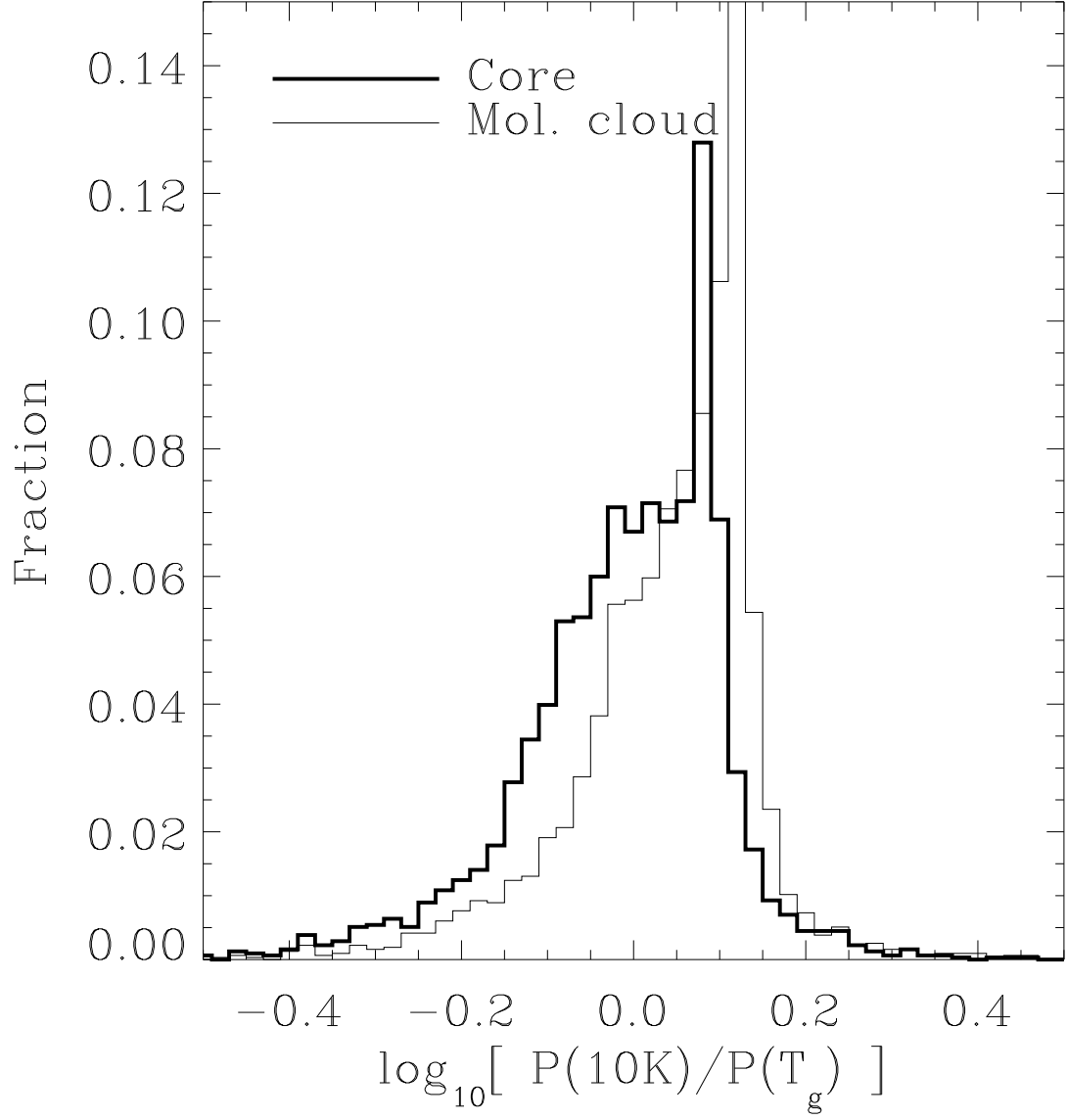


Fig. 9.— The discrepancy in polarization degrees obtained using the true grain temperatures,  $T_g$ , and holding them fixed at 10K. The binsize is 0.02dex.

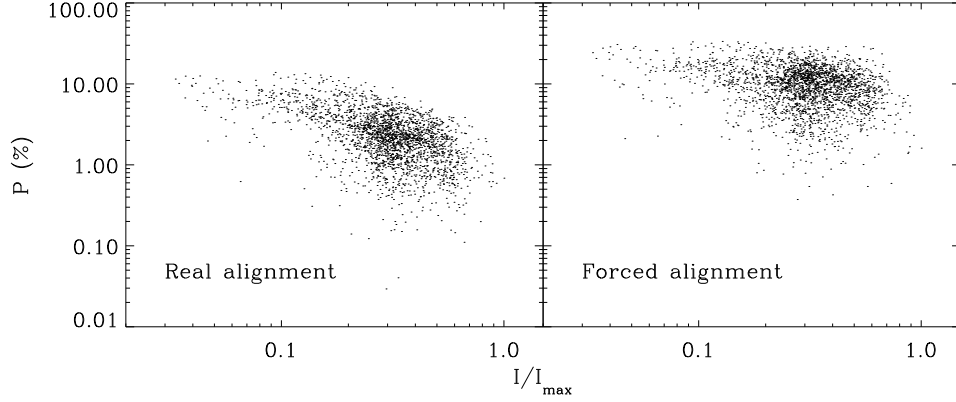


Fig. 10.— *Left*: The polarization degree,  $P$ , as a function of normalized intensity,  $I/I_0$ , for our molecular cloud model. *Right*: The P-I relation obtained when all silicate grains are forced into alignment with the magnetic field (*right*). Both are evaluated at  $850\ \mu\text{m}$ .

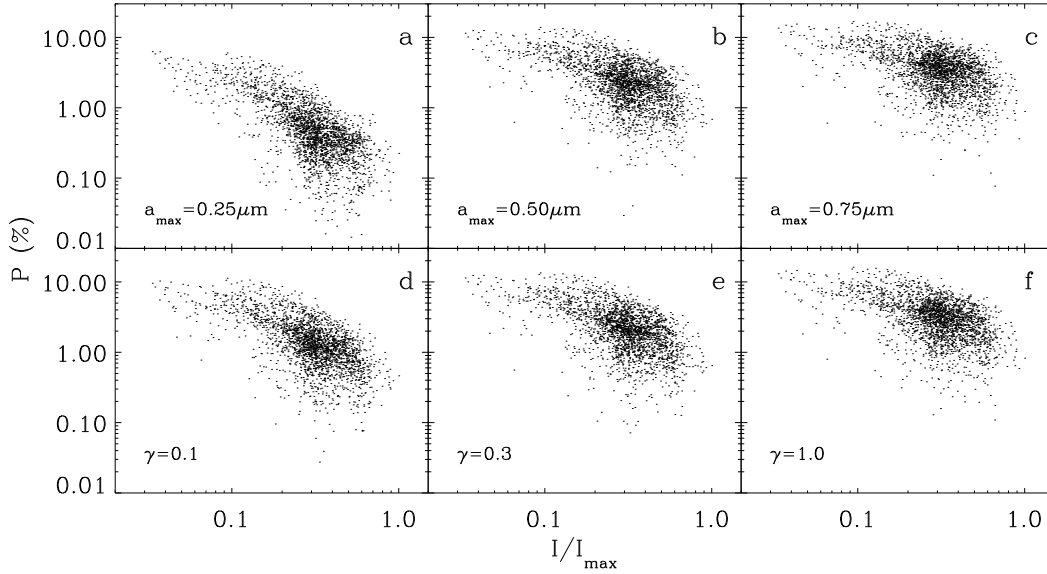


Fig. 11.— P-I plots for the model molecular cloud obtained from the parameter study. The top row (a-c) shows how varying the upper grain-size cutoff,  $a_{\text{max}}$ , changes the P-I relation. Plot *b* is in fact the result for our default molecular cloud. In the bottom row (d-f) we have replaced the real, spatially varying values for the radiative anisotropy,  $\gamma$ , with constant values  $\gamma = 0.1, 0.3$  and  $1.0$ .

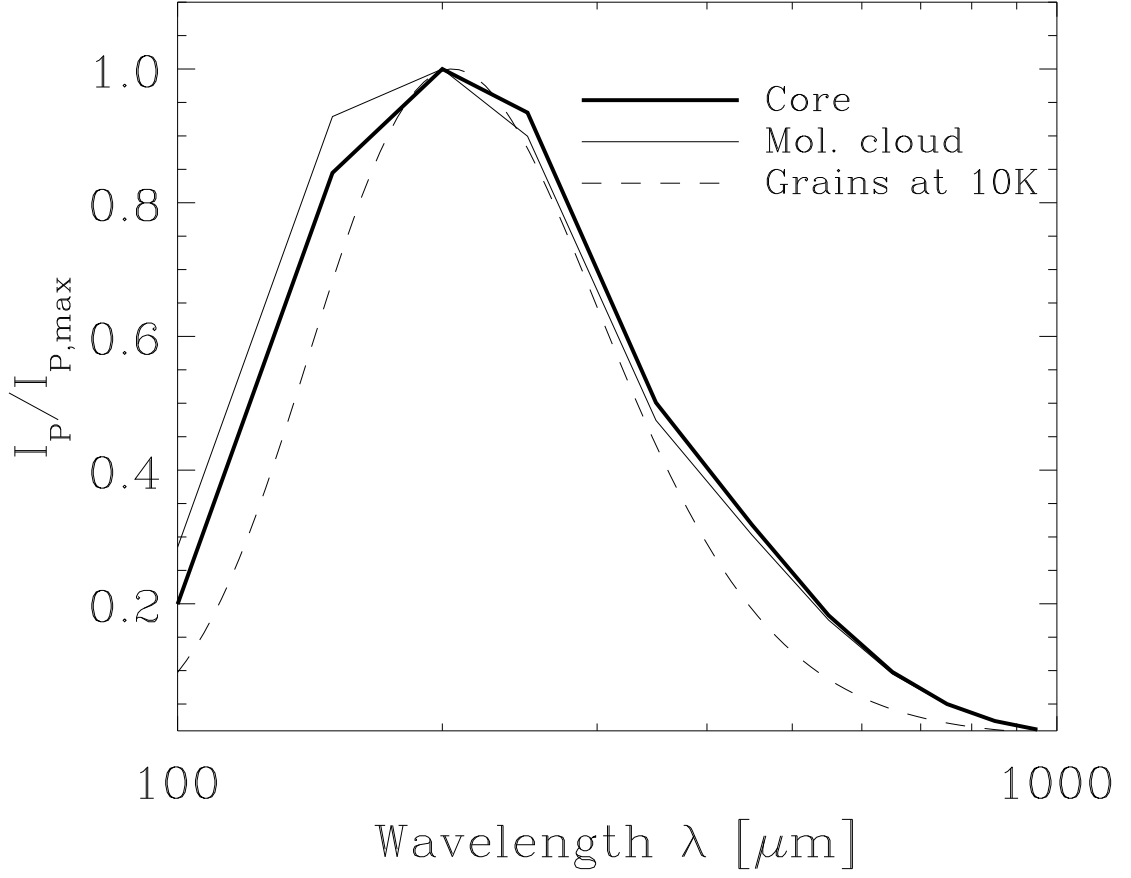


Fig. 12.— The normalized spectrum of the map-averaged polarized intensity,  $I_P$ , from our core (*thick solid line*) and molecular cloud (*thin solid line*) models. Also shown is a curve for grains with emission efficiencies  $\propto \lambda^{-2}$  emitting at a temperature of 10K (*dashed line*.)

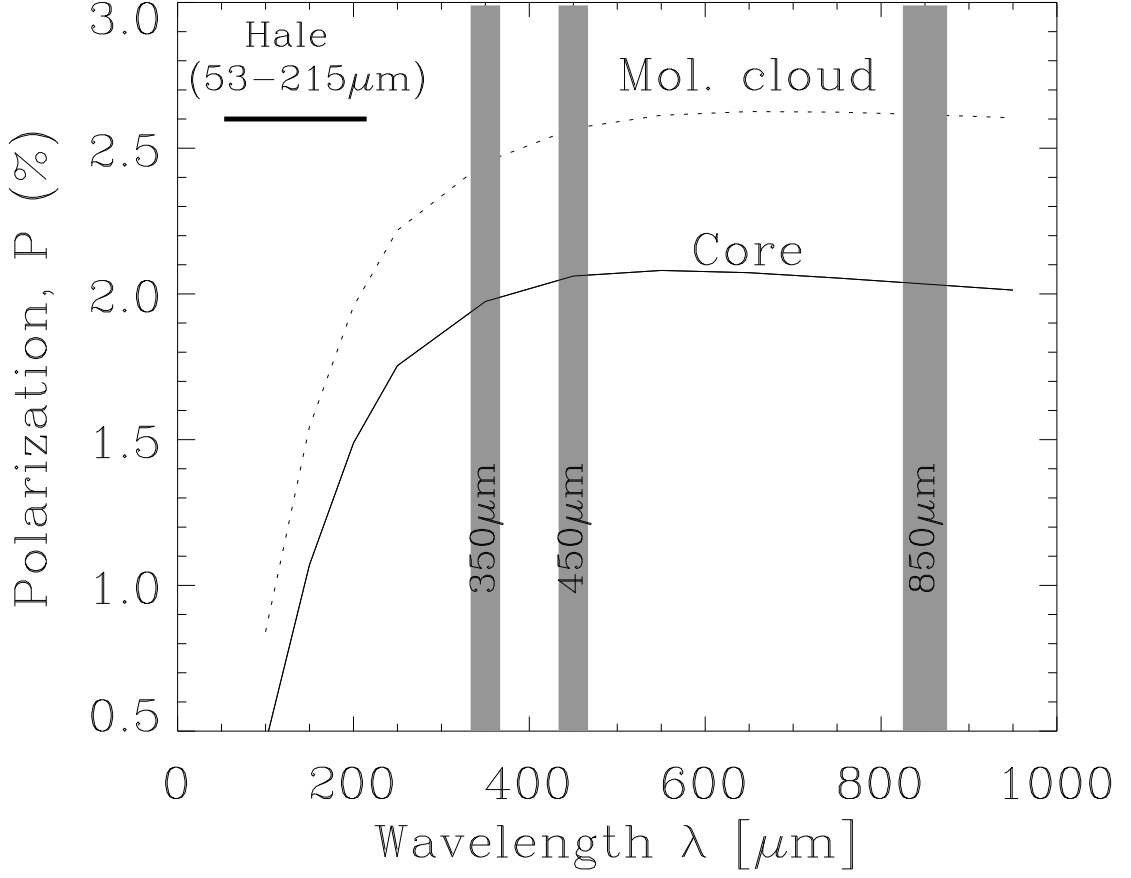


Fig. 13.— The polarization spectra of the model core (*solid line*) and molecular cloud (*dashed line*), overlaid with the "atmospheric windows" of relatively weak atmospheric water absorption centered at 350, 450 and 850  $\mu\text{m}$  (*shaded regions*). The projected Hale polarimeter waveband coverage is also shown. To calculate the polarization degree at a particular wavelength the total polarized emission,  $I_P$ , is integrated over the entire map and divided by the total map emission.

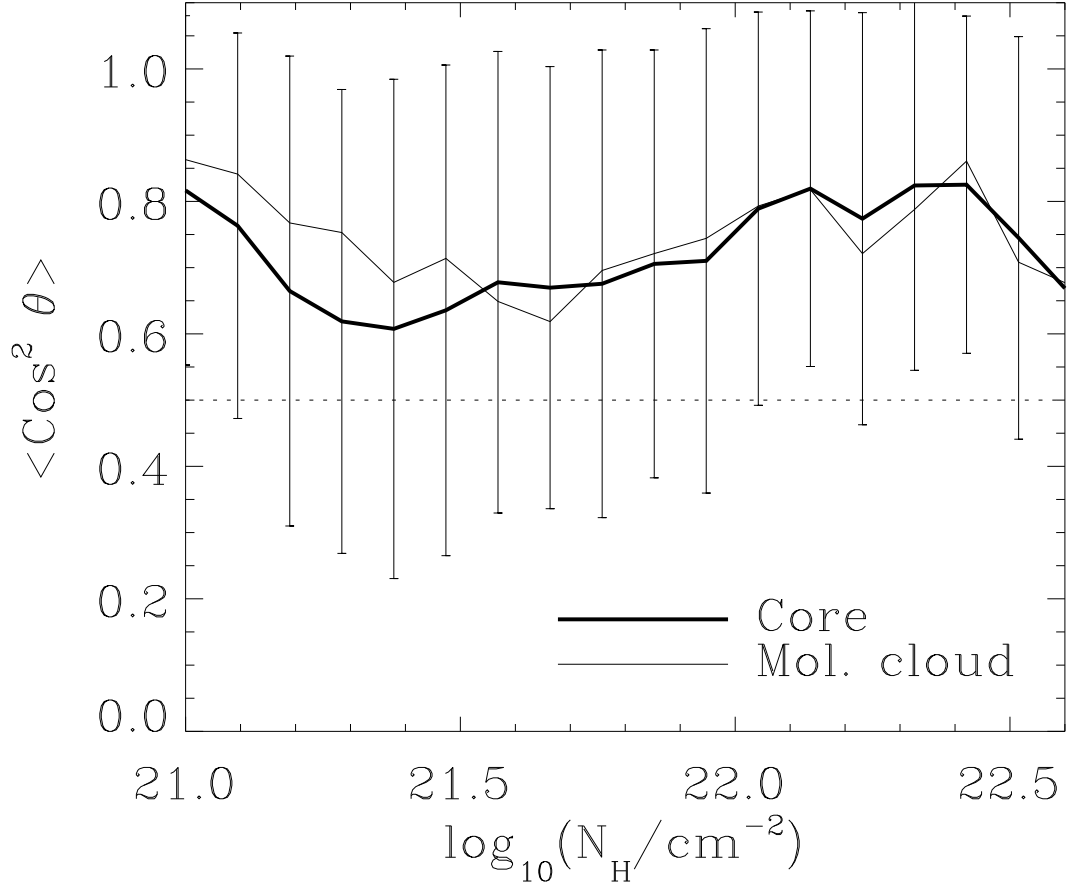


Fig. 14.— The mean squared cosine of the angle between polarization and projected magnetic field vectors,  $\langle \cos^2 \theta \rangle$ , as a function of column density. The error bars represent the r.m.s scatter about the mean. The polarization vectors at the default wavelength of  $850\mu\text{m}$  are used although there is little wavelength dependence of these quantities.

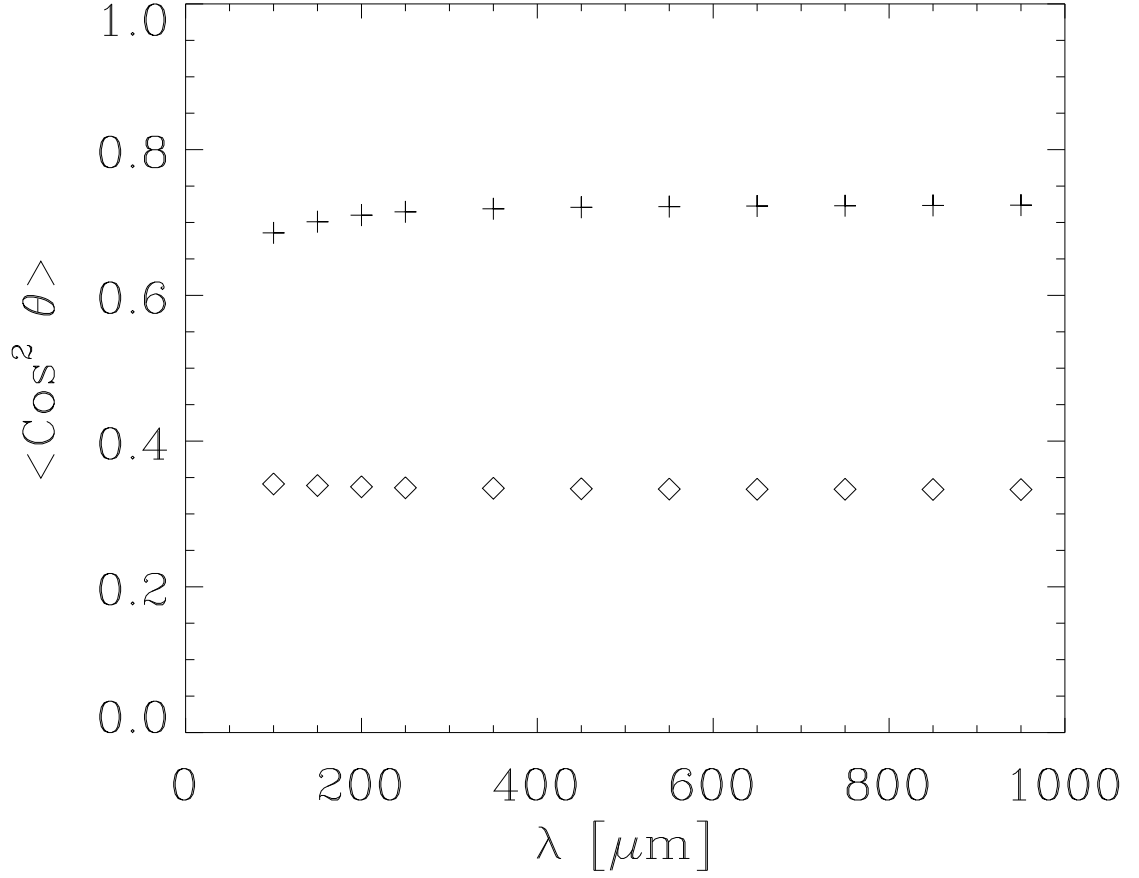


Fig. 15.— The mean squared cosine of the angle between polarization and projected magnetic field vectors,  $\langle \cos^2 \theta \rangle$ , Averaged over maps of our model core made at various wavelengths (*crosses*). The *diamonds* represent the root mean squared (*rms*) scatter about  $\langle \cos^2 \theta \rangle$ . The results for the molecular cloud model are almost identical and are not shown.